Efferocytosis of SARS-CoV-2-infected dying cells impairs macrophage anti-inflammatory programming and continual clearance of apoptotic cells

Douglas dos-Santos[1†], Ana C. G. Salina[1†], Tamara S. Rodrigues[1†], Marlon F. Rocha[1], Edismauro G. Freitas-Filho[1], Daniel L. Alzamora-Terrel[1], Mikhael H. F. de Lima[2], Daniele B. C. Nascimento[2], Ícaro Castro[3], Camila M. Silva[2], Juliana E. Toller-Kawahisa[2], Amanda Becerra[1], Samuel Oliveira[1], Diego B. Caetité[2], Leticia Almeida[1,4], Adriene Y. Ishimoto[1], Thais M. Lima[1], Ronaldo B. Martins[1], Flavio Veras[2], Natália B. do Amaral[5], Marcela C. Giannini[5], Letícia P. Bonjorno[5], Maria I. F. Lopes[5], Maira N. Benatti[5], Sabrina S. Batah, Rodrigo C. Santana[5], Fernando C. Vilar[5], Maria A. Martins[6], Rodrigo L. Assad[5], Sergio C. L. de Almeida[5], Fabiola R. de Oliveira[5], Eurico Arruda Neto[1], Thiago M. Cunha[2,4], José C. Alves-Filho[2,4], Fernando Q. Cunha[2,4], Alexandre T. Fabro[7], Helder Nakaya[3,4], Dario S. Zamboni[1,4], Paulo Louzada-Junior[5], Rene D. R. Oliveira[5], Larissa D. Cunha[1]*

[1]Departamento de Biologia Celular e Molecular e Bioagentes Patogênicos, Faculdade de Medicina de Ribeirão Preto, Universidade de São Paulo, Ribeirão Preto, SP, Brazil.
[2]Departamento de Farmacologia, Faculdade de Medicina de Ribeirão Preto, Universidade de São Paulo, Ribeirão Preto, São Paulo, Brazil.
[3]Departamento de Análises Clínicas e Toxicológicas, Faculdade de Ciências Farmacêuticas, Universidade de São Paulo, Brazil.
[4]Center of Research in Inflammatory Diseases (CRID), Faculdade de Medicina de Ribeirão Preto, Universidade de São Paulo, Ribeirão Preto, São Paulo, Brazil.
[5]Divisão de Imunologia Clinica, Emergência, Doenças Infecciosas e Unidade de Terapia Intensiva, Faculdade de Medicina de Ribeirão Preto, Universidade de São Paulo, Ribeirão Preto, SP, Brazil.
[6]Departamento de Cirurgia e Anatomia, Faculdade de Medicina de Ribeirão Preto, Universidade de São Paulo, Ribeirão Preto, SP, Brazil.
[7]Departamento de Patologia e Medicina Legal, Faculdade de Medicina de Ribeirão Preto, Universidade de São Paulo, Ribeirão Preto, SP, Brazil.

[†] D.S., A.C.G.S, and T.S.R. equally contributed to this work.

* Correspondence: Departamento de Biologia Celular e Molecular e Bioagentes Patogênicos
Faculdade de Medicina de Ribeirão Preto, Universidade de São Paulo
Av. Bandeirantes 3900, Ribeirão Preto, SP 14049-900, Brazil
Tel: +55 16 33153319
larissacunha@usp.br

Abstract

COVID-19 is a disease of dysfunctional immune responses, but the mechanisms triggering immunopathogenesis are not established. The functional plasticity of macrophages allows this cell type to promote pathogen elimination and inflammation or suppress inflammation and promote tissue remodeling and injury repair. During an infection, the clearance of dead and dying cells, a process named efferocytosis, can modulate the interplay between these contrasting functions. Here, we show that engulfment of SARS-CoV2-infected apoptotic cells (AC) exacerbates inflammatory cytokine production, inhibits the expression of efferocytic receptors, and impairs continual efferocytosis by macrophages. We also provide evidence that monocytes from severe COVID-19 patients express reduced levels of efferocytic receptors and fail to uptake AC. Our findings reveal that dysfunctional efferocytosis of SARS-CoV-2-infected cell corpses suppress macrophage anti-inflammation and efficient tissue repair programs and provide mechanistic insights for the pathogenesis of the hyperinflammation and extensive tissue damage associated with COVID-19.

KEYWORDS: COVID-19, macrophage, macrophage polarization, efferocytosis, hyperinflammation, tissue repair

Introduction

Because of its recent emergence, the pathogenesis of COVID-19 is still poorly defined. Patients with severe disease can progress to pneumonia, development of acute respiratory distress syndrome (ARDS) and respiratory failure, septic shock, and multiorgan dysfunction (*1*). These clinical manifestations of the disease have been associated with a dysregulated host immune response and compromised function of the myeloid compartment, suggesting that hyperinflammation and unresolved tissue damage could both contribute to the pathogenesis of severe COVID-19 (*2–8*).

Macrophages and monocytes promote disease tolerance and resolution of inflammation by sensing pathogen and host-derived pathogenic signals and programming their gene expression toward an anti-inflammatory, pro-resolution, and wound-healing phenotype (*9*). This host-protective programming reduces inflammatory cytokine production by other immune and non-immune cells and promotes the repair of damaged tissue to sustain physiological function and re-establish homeostasis (*10*). The efficient clearance of dying cells during the repair process prevents further tissue dysfunction caused by uncontrolled cytotoxicity and release of damage-associated molecular patterns (DAMP). Defects in sensing, ingesting, and degradation of dead and dying cells through efferocytosis cause chronic inflammation and autoimmune diseases (*11*). In addition to preventing the deleterious effects of secondary necrosis, efferocytosis also couples corpse internalization to other environmental cues (such as local cytokines and metabolites) to temporally and spatially regulate macrophage anti-inflammatory and tissue repair functions (*12*–

14). While the clearance of apoptotic cells is often associated with alternative macrophage programming, the identity of the dying cell, the type of cell death, and the context of death (either sterile or infectious) can modulate the nature of the macrophage response (*15*).

While infection with SARS-CoV2 induces the recruitment of immune cells to the lungs, their role in host defense and possible causes for the dysfunction during disease progression remain elusive. Here, we sought to determine how macrophages operate when responding to dying epithelial cells infected with SARS-CoV-2. We found that the presence of viable SARS-CoV-2 in cell corpses dysregulates macrophage anti-inflammatory responses to the efferocytosis of apoptotic cells. We show that the uptake of infected AC, and, to a lesser extent, infection of macrophages, impair the continual removal of cell corpses, a function prior known to promote effective wound repair. We also provide evidence the expression of efferocytic genes is reduced in COVID-19 patients with severe disease manifestation associated with hyperinflammation and that monocytes from severe patients are less efficient in the clearance of apoptotic cells. Therefore, SARS-CoV-2 infection and the clearance of infected dying cells disrupt macrophage host-protective functions associated with immunopathological manifestations of COVID-19.

Results

Macrophages engulf dying cells carrying viable SARS-CoV-2

Early reports demonstrate the cytopathic effect of SARS-CoV-2 infection in human and primate epithelial cells (*16, 17*). Analysis of immortalized epithelial cell lines (both human lung

epithelial Calu-3 and simian kidney epithelial Vero CCL81 cells) infected with SARS-CoV-2 revealed that dying cells exhibited features compatible with apoptosis, consistent with previous reports (*16–18*). (**Fig. 1A-C**). While lysis of infected epithelial cells can release virions (*16*, *17*), dying cells displayed increased intracellular positivity to an anti-Spike protein antibody (**Fig. 1 D** and **E**), suggesting that they may carry viable viral particles. To test this possibility, we performed the Median Tissue Culture Infection Dose (TCID50) assay, where we observed that viral particles isolated from dying Vero and Calu-3 apoptotic cells (CoV2-AC) induced cytopathic effect to an equivalent extent as those derived from supernatant (CoV2-AC Sup) (**Fig. 1F** and **G**). Therefore, viable SARS-CoV-2 is retained within infected dying epithelial cells.

Exposure of phosphatidylserine (PtdSer) on the outer plasma membrane of cells undergoing regulated cell death (RCD), as observed by annexin V-binding in CoV2-AC (**Fig. 1A**), is the most ubiquitous signal that triggers their phagocytosis (*19*, *20*). To determine whether SARS-CoV-2-infected dying cells are efficiently engulfed by phagocytes, we used flow cytometry to assess the uptake of CFSE-labelled, infected epithelial cells by macrophages differentiated from THP-1 monocytes. We observed that macrophages efficiently engulfed SARS-CoV-2- infected dying cells (**Figs. 1H-J**). We further confirmed the uptake of these infected corpses by confocal microscopy and staining for Spike protein in engulfed cells (**Fig. 1K**). Finally, efferocytosis of infected dying cells did not significantly affect the viability of macrophages up to 24 h post-treatment (**Fig. 1L**). These results demonstrate that macrophages engulf cell corpses carrying viable particles of SARS-CoV-2, offering a framework to investigate their effects on macrophage function.

Efferocytosis of SARS-CoV-2-infected dying cells impairs macrophage anti-inflammatory function

We next addressed the effect of the engulfment of SARS-CoV-2-infected, apoptotic cells (CoV2-AC) in macrophages. The uptake of sterile apoptotic cells often promotes macrophage functional polarization toward an anti-inflammatory and tissue repair phenotype (*21*). As expected, stimulation with UV-irradiated apoptotic Vero cells (UV-AC) increased both gene (**Fig. 2A**) and protein (**Fig. 2B** and **C; Fig. S1A** and **B**) expression of the mannose receptor C-type 1 (*MRC1*, *CD206*) in THP-1-derived macrophages, a hallmark of macrophage alternative programming to tissue remodeling and secretion of immune-modulatory mediators. However, upregulation of MRC1 at the gene or protein levels did not occur in response to stimulation with CoV2-AC (**Fig. 2A-C; Fig. S1A** and **B**). Stimulation with the supernatant of infected dying cells (containing putative DAMP and virions at approximately MOI of 0.01) or infection of macrophages themselves with SARS-CoV-2 at MOI of 1 did not induce *MRC1* transcription (**Fig. 2A**) or translation (**Fig. 2E**) in macrophages. We obtained similar results using primary monocyte-derived macrophages obtained from PBMC (**Fig. S1C-E**). To determine if viral viability was required for the modulation of CD206 expression by infected AC, CoV2-AC were exposed to UV irradiation. Macrophages that engulfed apoptotic epithelial cells containing inactivated SARS-CoV-2 exhibited increased CD206 surface expression, similar to that of UV-AC (**Fig. 2D**). This data suggests that alternative programming is actively repressed by viable SARS-CoV-2 carried in dying cells and is not primarily enforced by the type of cell death caused by the infection. Efferocytosis of UV-AC in the presence of SARS-CoV-2 still induced higher

expression of CD206 in macrophages (**Fig. 2E**), and therefore the suppression of the CD206 response required delivery of viral particles within corpses to macrophages.

We next examined the effect of cellular, SARS-infected cell corpses to regulate cytokine production by macrophages after engulfment. In contrast to the engulfment of UV-AC, we observed that the uptake of CoV2-AC significantly increased *IL6* expression (**Fig. 2F**). While direct infection of macrophages with SARS-CoV-2 increased *IL6* transcription, efferocytosis of CoV2-AC induced a much stronger response (**Fig. 2F**). The uptake of CoV2-AC also induced robust secretion of inflammatory IL-6 (**Fig. 2G-I**) and IL-1β (**Fig. 2J-L**), in both THP1- and PBMC-derived macrophages. We did not detect these cytokines in macrophages stimulated with the supernatant from infected cells, and therefore this effect was not due to infection from dying epithelial cells nor by free viral particles or released DAMPs (**Fig. 2G-L**). Further, the induction of inflammatory cytokines by SARS-CoV-2-loaded corpses required the presence of viable viral particles, as UV-treatment or paraformaldehyde-fixation of infected corpses abrogated IL-6 secretion (**Fig. 2M**). Collectively, our findings provide evidence that engulfment of dying cells carrying viable SARS-CoV-2 switches the anti-inflammatory, resolutive programming in response to efferocytosis toward an inflammatory phenotype. The exacerbate cytokine production observed in response to the efferocytosis of infected corpses by macrophages may contribute to the hyperinflammation associated with COVID-19.

Efferocytosis of SARS-CoV-2-infected dying cells suppresses continual clearance of apoptotic cells

Several receptors mediate efferocytosis through recognition of PtdSer on the surface of a dying cell, either by direct binding or through a bridging molecule (*11*, *22*). Interestingly, engulfment of CoV2-AC by macrophages reduced the transcription of such PtdSer receptors, including the scavenger receptors *CD36* (**Fig. 3A**) and *SRA-I* (**Fig. 3B**), *αVβ5* integrin (*ITGB5*) (**Fig. 3C),** and T cell immunoglobulin mucin receptor 4 (*TIM4*) (**Fig. 3D**), but not MER proto-oncogene tyrosine kinase (*MERTK*) (**Fig. 3E**). We also observed reduced expression of *SRA-I*, *ITGB5*, and *TIM4* receptors in response to CoV2-AC supernatant or infection with SARS-CoV-2 at MOI of 1 (**Fig. 3A-D**). Phagocytes can ingest multiple corpses in subsequent rounds of efferocytosis (*23–26*). Previous *in vivo* work showed that macrophages must continually remove ACs to promote efficient repair of injury and prevent the accumulation of secondarily necrotic cells (*25*, *27*). To determine if repression of efferocytic receptors affects additional uptake of dying cells, we treated macrophages with CoV2-AC, and, subsequently fed them with UV-AC. We found that engulfment of a SARS-CoV-2-infected corpse suppressed the efferocytosis of other apoptotic cells (**Fig. 3F**). As infection with SARS-CoV-2 reduced the expression of efferocytic receptors (**Fig. 3A-D**), we also tested if it affected the uptake of apoptotic cells. Comparatively, infection with SARS-CoV-2 reduced AC clearance to a lower extent than that of prior uptake of CoV2-AC (**Fig. 3G**). Thus, efferocytosis of SARS-CoV-2-infected, dying cells affects the expression of efferocytic receptors and impairs the continual removal of apoptotic cells by macrophages.

Efferocytosis is impaired in monocytes from COVID-19 patients

To explore the contribution of dysfunctional efferocytosis in COVID-19 pathophysiology, we profiled the monocyte population in blood samples from 26 moderate to severe patients on the day of hospitalization (**Table S1**). Assessment of circulating cytokines confirmed higher levels of IL-6, IL-8, IL-10, and IL-1β in this cohort of patients (**Fig. S2A-F**)(*5*, *7*). We observed an increase in the absolute numbers of circulating monocytes and the proportion of monocytes among total leukocytes in COVID-19 patients when compared to healthy control (HC) volunteers (**Fig. S2G-I**), as described (*5*). These cells also expressed less human leukocyte antigen DR isotype (HLA-DR) on their surface (**Fig. S2J**), as described (*5*, *6*). We observed changes in monocytes subsets in COVID-19 patients, with an increase in the percentage of intermediate, inflammatory monocytes ($CD14^{hi}$ $CD16^{+}$) and a reduction in non-classical, anti-inflammatory monocytes ($CD14^{int}$ $CD16^{+}$) that execute efferocytosis more efficiently (**Fig. 4A-C**), similar to other observations (*3*, *6*, *28*). We then assessed the expression of CD36, a lipid-binding receptor with affinity for anionic phospholipids such as PtdSer exposed on dying cells (*29*, *30*), and found reduced surface expression on monocytes of COVID-19 patients, compared to healthy controls (**Fig. 4D-F**).

We next recovered the PBMC blood fraction from 42 moderate or severe COVID-19 patients by density gradient separation and evaluated the expression of efferocytic receptors by qPCR. Similar to our previous findings, we observed lower expression of *CD36*, *SRA-I*, *ITGB5*, and *TIMD4*, but not *MERTK*, in PBMC from COVID-19 patients when compared to HC (**Table S1, Fig. 4G-K**). We then addressed a possible association between the levels of efferocytic receptors and the worsening of COVID-19. To that end, we stratified the patients according to their hyperinflammatory state at hospital admission, based on a recently proposed score of

clinical criteria (fever, macrophage activation, hematological dysfunction, coagulopathy, hepatic injury, and cytokinaemia) that defines COVID-19-associated hyperinflammation (cHIS score) (*31*). We found a statistically significant reduction in the expression of *CD36*, *TIMD4*, and *SRA-I* for patients with a cHIS score of at least 2, which is associated with worsening in severity and risk of death (*31*) (**Fig. 4L-N**).

Finally, we assessed the uptake of dying cells by monocytes from COVID-19 patients. We stimulated monocytes obtained from PBMC samples from COVID-19 patients with apoptotic murine thymocytes and evaluated their phagocytic activity by epifluorescence microscopy. We found that monocytes from COVID-19 patients were less efficient in the uptake of dying cells (**Fig. 4O** and **P**). This failure was not caused by an intrinsic defect in phagocytosis, as monocytes from HC and COVID-19 patients internalized zymosan similarly (**Fig. 4Q**). Thus, monocytes from severe COVID-19 patients that develop hyperinflammation express lower levels of efferocytic receptors and are less efficient in the clearance of dying cells.

Lung-infiltrating monocytes and macrophages of COVID-19 patients express reduced levels of efferocytic receptors

As we found a reduction in the expression of efferocytic receptors and a failure in the engulfment of dying cells in circulating monocytes of COVID-19 patients, we then examined efferocytosis in the lungs of these patients. Using publicly available single-cell RNA sequencing (RNA-seq) data from bronchoalveolar lavage (BAL)(*32*), we first performed differentially expressed gene (DEG) analysis comparing mild and severe COVID-19 patients and HC. In the

clusters identified as early infiltrating phagocytes (S1009^{+} CCL18^{-}) and anti-inflammatory monocyte-derived macrophages (CD14^{+} S11009^{-} CCL18^{+}), we examined the expression of genes related to the different stages of efferocytosis (regulation of engulfment, 'find-me' receptors, recognition 'eat-me' receptors, and regulation of phagosome maturation in the clearance of apoptotic cells), according to gene ontology annotation 'apoptotic cell clearance' (GO:0043277) and the literature (*11*, *22*). Our analysis identified reduced expression of several genes associated with engulfment and recognition receptors in severe COVID-19 compared to those with mild disease (**Fig. 5A**).

We further assessed the expression of efferocytic receptors by immunofluorescence in lung tissues obtained from autopsies of deceased COVID-19 patients. We found a reduction in the protein levels of CD36 in S1009^{+} cells (representing early infiltrating monocytes and monocyte-derived macrophages) in the lungs of COVID-19 patients when compared to control tissues (**Fig. 5B** and **C**). Phagocytes in the lungs of COVID-19 patients also expressed lower protein levels of MERTK (**Fig. 5C** and **D**), although transcription of *MERTK* was not reduced in their circulating PBMC (**Fig. 4K**). Altogether, these data suggest that infiltrating monocyte and monocyte-derived macrophages that differentiate in the lungs of COVID-19 patients may also fail in their efferocytic capacity.

Discussion

In summary, we demonstrate that the engulfment of SARS-CoV-2-infected dying cells by macrophages switches the effector response to efferocytosis from a potential wound healing,

anti-inflammatory function to a pro-inflammatory one. An important consequence of this shift is the impairment of macrophage capacity to continually engulf apoptotic cells and promote proper resolution of injury; instead, our data suggest that efferocytosis of infected cells may augment tissue damage by causing inefficient clearance of dead cells. Our data showing lower levels of efferocytic receptors in lung-infiltrating monocytes and macrophages in severe COVID-19 cases, together with the demonstration that circulating monocytes of COVID-19 patients fail in the uptake of dying cells, suggest that impaired efferocytosis may contribute to the accumulation of dead cells and extensive tissue damage observed in the lungs of COVID-19 patients. This may consequently contribute to respiratory complications developed by patients with the severe form of the disease and increase susceptibility to secondary bacterial infections for the lack of effective disease tolerance mechanisms that restrain collateral tissue damage (*33*). In the context of COVID-19 immunopathogenesis, excessive amounts of necrotic cells may lead to high levels of circulating DAMP such as HMGB1 and lactate dehydrogenase (LDH), both of which correlate with disease severity(*7*, *34*, *35*). It is thus possible that the combination of exacerbated cytokine production and interruption of continual efferocytosis in response to engulfment of SARS-CoV-2-infected corpses could both increase the magnitude and duration of inflammation, contributing to the hyperinflammatory state and multiorgan damage in COVID-19. Finally, recent studies reported higher levels of autoantibodies (such as against IFNγ, phospholipids, and annexin A2) in COVID-19 patients (*36*–*38*), suggesting that autoantibodies may drive the worsening of the disease. It has long been known that defective engulfment or processing of dying cells causes the development of autoimmune diseases (*11*, *26*, *39*–*42*). In light of our findings, perhaps defective clearance of apoptotic cells caused by SARS-CoV-2 infection and SARS-CoV-2-loaded ACs also contributes to COVID-19-associated autoimmunity.

As it becomes clear that COVID-19 is a disease of immune dysfunction (*40*), antivirals, and other therapeutic efforts to limit viral replication may fail to benefit critically ill patients. In those patients, successful therapeutic strategies may rely on targeting dysregulated components of the host response to limit damage to the host, thus promoting disease tolerance and stimulating a resolutive response that restores homeostasis. In this context, our study provides important insights into the mechanisms driving the pathophysiology of COVID-19 that can be explored in the design of therapeutics approaches toward harnessing innate immune responses and macrophage function during SARS-CoV-2 infection.

Material and Methods

Study approval. The procedures followed in the study were approved by the Research Ethics Committee of Hospital das Clínicas de Ribeirão Preto (CEP-FMRP/USP) and by the National Ethics Committee, Brazil (Comissão Nacional de Ética em Pesquisa (CONEP), protocols 30248420.9.0000.5440 and 39722020.9.0000.5440. Written informed consent was obtained from recruited patients.

Patient samples. A total of 59 patients with COVID-19 (confirmed by RT-PCR as previously described (*43*) participated in this study. Patients were stratified according to their clinical manifestations in (1) mild cases, in which there are mild clinical symptoms and no pneumonia is found in imaging; (2) moderate cases, characterized by fever, respiratory tract symptoms, and pneumonia is identified in imaging; and (3) severe cases, in which adults presented any of the

following features: arterial partial pressure of oxygen (PaO_2)/oxygen concentration (FiO_2) <300 mm Hg, oxygen saturations 93% at a rest state and respiratory rate >30 breaths/min. Samples were collected from patients admitted in Hospital das Clínicas, Faculdade de Medicina de Ribeirão Preto da Universidade de São Paulo from April to August of 2020. **Table S1** describes clinical, laboratory, and treatment records of COVID-19 patients. Samples from healthy donors tested negative for COVID-19 using RT-PCR and/or tested negative using serology (specific IgM and IgG antibodies; Asan Easy Test COVID-19 IgM/IgG kits, Asan Pharmaceutical Co.) were used as controls.

Peripheral blood mononuclear cells isolation. Peripheral blood mononuclear cells (PBMC) from healthy donors and COVID-19 patients were collected in tubes containing EDTA (BD Biosciences). The samples were centrifuged at 400 x g for 10 min at room temperature (RT), the plasma was discarded, and the cell pellet was resuspended in phosphate-buffered saline (PBS). PBMC were isolated by density – gradient centrifugation using Histopaque-1077 (Sigma-Aldrich). Collected cells were washed with PBS and resuspended in RPMIc prior to further use.

Cells. Jurkat, Calu-3, Vero CCL81, and THP-1 cells were from (ATCC®). Thymocytes were obtained from from C57BL/6 mice. Jurkat cells and murine thymocytes were maintained in RPMI1640 (GIBCO) media (RPMIc) (supplemented with penicillin 10,000 U/mL, streptomycin 10,000 μg/mL and 10% heat-inactivated fetal bovine serum (FBS)) at 37°C in a 5% CO_2 atmosphere. Calu-3 and Vero CCL81 cells were maintained in complete DMEM (GIBCO) (DMEMc) (supplemented with penicillin 10,000 U/mL, streptomycin 10,000 μg/mL and 10% FBS) at 37°C in a 5% CO_2 atmosphere. THP-1 cells were maintained in RPMIc. THP-1-derived

macrophages were obtained by treatment with 50ng/mL of phorbol 12-myristate 13-acetate (PMA) (Sigma-Aldrich, San Luis, Missouri, USA) for 24h, followed by media replenishment with fresh RPMIc and other 24h incubation.

Viral stock. The SARS-CoV-2 strain (Brazil/SPBR-02/2020) was isolated from the first Brazilian case of COVID-19. Viral stock was propagated under BSL3 conditions and stored at -80°C. The viral stock was produced in a monolayer of Vero CCL81 cells cultured in serum-free DMEM (GIBCO) at 37°C in a 5% CO_2 atmosphere.

Apoptosis induction. Apoptotic cells (UV-AC) were generated by exposure to UV radiation, followed by 6h incubation in complete media at 37°C in a 5% CO_2 atmosphere: apoptotic thymocytes and Jurkat cells at 20 mJ, Calu-3 cells at 500 mJ and Vero CCL81 cells at 350 mJ. To generate infected apoptotic Vero CCL81 and Calu-3 cells (CoV2-AC), cells were incubated with SARS-CoV-2 at a multiplicity of infection (MOI) of 1 in serum-free media for 1h for viral adsorption, topped with fresh DMEM and incubated for 48h. Detection of PtdSer by annexin-V-labelling (APC annexin-V, BD Biosciences) and detection of intracellular cleaved caspase-3 (Cell Signaling) and secondary donkey anti-rabbit IgG conjugated to Alexa Fluor 488 (AF488, Molecular Probes) were analyzed by flow cytometry.

Determination of viable viral particles. Spike$^+$ cells were estimated by flow cytometry using monoclonal rabbit anti-SARS-CoV-2 spike protein (ThermoFisher Scientific) and secondary donkey anti-rabbit IgG conjugated to Alexa Fluor 647 (AF647, Molecular Probes).

Viral loads in CoV2-AC corpses and in the supernatant from CoV2-AC were estimated by titration in Vero CCL81 cell culture on 96-well plate and expressed as 50% tissue culture infectious dose (TCID50). Quantification was performed with Reed-Muench method and plotted in TCID50 units per mL (*44*)

***In vitro* assays with THP-1- and PBMC-derived macrophages.** THP-1- and PBMC-derived macrophages seeded on tissue-culture 24 well plates were incubated with UV-AC or CoV2-AC at 1:1 ratio, stimulated with the supernatant of CoV2-AC, or infected with SARS-CoV-2 at a MOI of 1 for 24h. After that, the cells were collected for evaluation of CD206 surface expression by flow cytometry (using anti-CD206 antibody clone 19.2, FITC - BD Biosciences) or gene expression analysis by RT qPCR, and the supernatant of the culture was collected for cytokine quantification (as described below). As indicated in the figure legends, CoV2-AC cells and the supernatant of these cells were treated with UV for 20 min or fixed using 2% PFA prior to incubation with macrophages.

For efferocytosis imaging, THP1-derived macrophages plated on slide chambers were stimulated with UV-AC or CoV2-AC for 4h at 1:1 ratio, washed with PBS and fixed with 4% of paraformaldehyde (PFA). Cells were permeabilized with 0.1% Triton-X-100 in PBS for 10 min at RT and slides were blocked with 1% bovine serum albumin (BSA), 5 µg/uL rat IgG in PBS for 45 min RT prior to overnight incubation with monoclonal rabbit anti- SARS-CoV-2 spike antibody in blocking buffer. Slides were washed with PBS, incubated with secondary donkey anti-rabbit IgG conjugated to Alexa Fluor 647 (ThermoFisher Scientific) for 1h, stained with Hoechst 33342. Slides were then rinsed, and coverslips mounted with Fluoromount-G

(Invitrogen). Immunofluorescence images were obtained with a LEICA TCS-NT SP5 laser scanning confocal microscope (Leica Microsystems).

For the efferocytosis assays by flow cytometry, THP-1 cells were labelled with 1 µM CellTrace™ FarRed dye (Thermo Scientific), according to the manufacturer's recommendations, prior to macrophage differentiation. FarRed-labelled THP-1-derived macrophages were stimulated with UV-AC or CoV2-AC previously stained with 5 µM CellTrace™ CFSE dye (Thermo Scientific), at 1:1 ratio for 2h. For the two-round efferocytosis assay, THP-1 cells were labelled with 5 µM CellTrace™ Violet dye (Thermo Scientific). First-round UV-AC and CoV2-AC were labelled with a pH indicator fluorogenic intracellular probe (pHrodo Red AM Intracellular pH Indicator - Thermo Scientific). Second-round UV-AC were labelled with 1 µM CellTrace™ FarRed dye. Briefly, Violet-THP-1 cells were incubated with UV-AC-pHrodo or CoV2-AC-pHrodo for 18h at 1:1 ratio. Cells were then washed 3 times with PBS to remove non-engulfed cells and FarRed-UV-AC were added to the culture at 1:1 ratio for 2h. The percentage of apoptotic cell uptake was evaluated in both cases by flow cytometry.

***In vitro* efferocytosis assay with monocytes from COVID-19 patients.** PBMC from healthy donors or COVID patients were plated onto eight-well chamber slides (Tek Chamber Slide, Thermo Scientific) in serum-free media for 1h at 37ºC in a 5% CO_2 atmosphere for monocyte adherence. Next, cells were washed 2x with PBS to remove non-adherent cells and incubated in RPMIc overnight. Monocytes were cultured with apoptotic thymocytes for 1h or zymosan A particles (Thermo Scientific) for 20 min at 37°C in a 5% CO_2 atmosphere. The cells were then thoroughly washed with PBS, fixed in 4% PFA for 15 min and rinsed 2x with 0.01% Tween-20

Tris-buffered saline (TBS). After permeabilization (0.1% Triton-X-100 in TBS for 3 min at RT), cells were labelled with phalloidin conjugated to Alexa Fluor 488 (Thermo Scientific) and Hoechst 33342, and coverslips mounted with Fluoromount-G. Immunofluorescence images were obtained using the Leica DMI4000B microscope (Leica Microsystems; Heidelberg, Germany). The representative images were obtained using a Zeiss LSM 780 laser scanning confocal microscope (Carl Zeiss, Heidelberg, Germany).

Flow cytometric analyses. For the analysis of cleaved caspase-3 and Spike in Vero CCL81 and Calu-3 infected with SARS-Cov-2, cells were fixed, permeabilized and stained using BD Cytofix/Cytoperm™ Fixation/Permeabilization Kit (BD Biosciences), following the manufacturer's directions.

For the analysis of THP-1- and PBMC-derived macrophages stimulated *in vitro*, cells were labelled with Zombie Violet™ Fixable Viability Kit (Biolegend Inc., San Diego, CA, USA) and labelling probes or antibodies described above. Surface staining was carried out for 15 minutes at 4°C.

For phenotyping of blood circulating monocytes, blood samples from healthy donors and COVID-19 patients were processed for lysis of red blood cells, followed by labelling with monoclonal antibodies for CD14 (clone M5E2; BD Pharmingen™), CD16 (clone ebioCB16(CB16); eBioscience Inc., San Diego; CA, USA), CD36 (clone CB38; BD Pharmingen™) and Fixable Viability Dye eFluor 780 (eBioscience) for 30 min at 4°C.

All flow cytometric analyses were performed in a FACSVerse (BD Biosciences, San Jose, CA, USA) flow cytometer.

Cytokine quantification. The IL-6 cytokine levels in supernatant culture were evaluated by ELISA assay (R&D Systems, Minneapolis, MN, EUA) or BD™ Cytometric Bead Array (CBA) (BD Biosciences), following the manufacturers' recommendations. IL-1β, IL-6, IL-8, IL-10, IL-12, and TNF-α detection in serum from healthy donors and patients with COVID-19 were performed with CBA.

RNA isolation and gene expression analyses. The total RNA extraction of PBMC from healthy donors or COVID-19 patients was made using PureLink™ RNA Mini Kit (Ambion Inc., ThermoFisher Scientific), following the manufacturer's recommendations. Reverse transcription was performed using the High Capacity cDNA Reverse Transcriptase Kit (Applied Biosystems™, Foster City, Ca, USA), following the manufacturer's recommendations.

Total RNA extraction for PBMC or THP-1-derived macrophages stimulated *in vitro* was performed using Directzol™ RNA miniPrep Kit (Zymo Research, Irvine, CA, USA), following the manufacturer's recommendations. Reverse transcriptase was performed using M-MLV reverse transcriptase (ThermoFisher Scientific) according to the manufacturer's recommendations.

Gene expression qRT-PCR was performed using SybrGreen Master Mix (Applied Biosystems, Foster City, CA, USA). qRT-PCR was performed in a fast mode, following the manufacturer's

recommendations. The evaluation of each gene expression was determined by the comparative CT method. Primer sequences used:

Gene	Primer Forward	Primer Reverse
CD36	GGGAAAGTCACTGCGACATG	TGCAATACCTGGCTTTTCTCA
GAPDH	GTCTCCTCTGACTTCAACAGCG	ACCACCCTGTTGCTGTAGCCAA
IL6	GGTACATCCTCGACGGCATCT	GTGCCTCTTTGCTGCTTTCAC
ITGB5	AACCAGAGCGTGTACCAGAA	AGGAGAAGTTGTCGCACTCA
MERTK	CTCTGGCGTAGAGCTATCACT	AGGCTGGGTTGGTGAAAACA
MRC1	AGCCAACACCAGCTCCTCAAGA	CAAAACGCTCGCGCATTGTCCA
SRA-1	GCAGTGGGATCACTTTCACAA	AGCTGTCATTGAGCGAGCATC
TIM4	ACAGGACAGATGGATGGAATACCC	AGCCTTGTGTGTTTCTGCG

Re-analysis of scRNA-seq Data. We analyzed single-cell transcriptomic data from bronchoalveolar lavage fluid (BALF) from patients with varying severity of COVID-19 disease and their respective healthy controls (*32*). The dataset is publicly available at https://covid19-balf.cells.ucsc.edu/. Basically, the dataset was downloaded and the RDS file was imported into R environment version v3.6.3. Differential expression analysis was conducted using FindMarkers function in Seurat using Wilcoxon test to compare mild and severe COVID-19 patients with healthy individuals for each cluster previously identified by authors. Differentially expressed genes between mild/severe COVID-19 patients and controls for each cluster were identified considering genes expressed in at least 5% of cells and FDR < 0.05 and |avg_logFC| > 0.1.

Histological analysis. Autopsies from COVID-19 patients and non-COVID-19 patients were performed using the ultrasound-guided minimally invasive approach (Veras et al., 2020). Fragments of the lung were collected and processed as previously described (Rodrigues et al., 2020). Non-neoplasic samples of lung parenchyma were obtained from lobectomies for lung

cancer as a control group. Sections from lungs were washed in PBS and the antigen retrieval was performed by incubation of samples in PBS with 0.1% trypsin (ThermoFisher Scientific) at 37ºC for 15 min. Then, samples were washed and incubated with Image-iT FX Signal Enhancer (ThermoFisher Scientific) for 30 min at RT. Next, sections were washed with PBS and incubated for 45 min at RT in PBS containing 0.5% BSA and normal donkey IgG (5µg/mL; Jackson ImmunoResearch, West Grove, PA, USA). Lung sections were labeled with primary antibodies rabbit anti-Human CD36 (ThermoFisher Scientific), rabbit anti-Human MERTK (ThermoFisher Scientific) and mouse anti-Human Calprotectin (ThermoFisher Scientific) diluted in PBS overnight at 4ºC. Then, sections were washed thoroughly in PBS and incubated for 45 min at RT with the secondary antibodies donkey anti-rabbit IgG conjugated to Alexa Fluor 488 (Jackson ImmunoResearch) and goat anti-mouse IgG conjugated to Alexa Fluor 594 (Jackson ImmunoResearch) diluted in PBS. Sections were then rinsed, and coverslips mounted with DAPI Fluoromount-G (EM Sciences, Hatfield, PA, USA). The images were obtained using the Olympus BX61 Fluorescence Motorized Slide Scanner Microscope Pred VS120 (Olympus, Hamburg, Germany). Minimally invasive autopsies for COVID-19 deceased patients were approved by the Research Ethics Committee of Hospital das Clínicas de Ribeirão Preto (CEP, protocol no. 4.089.567).

Data processing, quantification and statistical analyses. Flow cytometric data processing was performed using FlowJo_V10 software (BD Biosciences). Images obtained by confocal and epifluorescence microscopy were analyzed using ImageJ (NIH). Data were plotted and analyzed with GraphPad Prism 8.4.2 software (GraphPad Prism Software Inc., San Diego, CA). The statistical tests used are listed in the figure legends. For *in vitro* assays, we used Student's t-test

to compare two experimental groups or one-way ANOVA, followed by ordinary ANOVA and multiple comparison correction, to compare three or more experimental groups. For the comparison between COVID-19 patients and healthy control datasets, normality tests were performed and samples with non-Gaussian distribution were analyzed applying Mann–Whitney test. For monocyte phenotyping from blood samples, the outliers were identified applying the ROUT method defining Q = 0,1% and then removed from the analyses. p values < 0.05 were considered significant.

References

1. H. K. Siddiqi, M. R. Mehra, COVID-19 Illness in Native and Immunosuppressed States: A Clinical-Therapeutic Staging Proposal. *J Hear Lung Transplant* (2020), doi:10.1016/j.healun.2020.03.012.

2. D. M. D. Valle, S. Kim-Schulze, H.-H. Huang, N. D. Beckmann, S. Nirenberg, B. Wang, Y. Lavin, T. H. Swartz, D. Madduri, A. Stock, T. U. Marron, H. Xie, M. Patel, K. Tuballes, O. V. Oekelen, A. Rahman, P. Kovatch, J. A. Aberg, E. Schadt, S. Jagannath, M. Mazumdar, A. W. Charney, A. Firpo-Betancourt, D. R. Mendu, J. Jhang, D. Reich, K. Sigel, C. Cordon-Cardo, M. Feldmann, S. Parekh, M. Merad, S. Gnjatic, An inflammatory cytokine signature predicts COVID-19 severity and survival. *Nat Med*. **26**, 1636–1643 (2020).

3. A. Silvin, N. Chapuis, G. Dunsmore, A.-G. Goubet, A. Dubuisson, L. Derosa, C. Almire, C. Hénon, O. Kosmider, N. Droin, P. Rameau, C. Catelain, A. Alfaro, C. Dussiau, C. Friedrich, E. Sourdeau, N. Marin, T.-A. Szwebel, D. Cantin, L. Mouthon, D. Borderie, M. Deloger, D. Bredel, S. Mouraud, D. Drubay, M. Andrieu, A.-S. Lhonneur, V. Saada, A. Stoclin, C. Willekens, F. Pommeret, F. Griscelli, L. G. Ng, Z. Zhang, P. Bost, I. Amit, F. Barlesi, A. Marabelle, F. Pène, B. Gachot, F. André, L. Zitvogel, F. Ginhoux, M. Fontenay, E. Solary, Elevated Calprotectin and Abnormal Myeloid Cell Subsets Discriminate Severe from Mild COVID-19. *Cell*. **182**, 1401-1418.e18 (2020).

4. D. Blanco-Melo, B. E. Nilsson-Payant, W.-C. Liu, S. Uhl, D. Hoagland, R. Møller, T. X. Jordan, K. Oishi, M. Panis, D. Sachs, T. T. Wang, R. E. Schwartz, J. K. Lim, R. A. Albrecht, B. R. tenOever, Imbalanced Host Response to SARS-CoV-2 Drives Development of COVID-19. *Cell*. **181**, 1036-1045.e9 (2020).

5. C. Lucas, P. Wong, J. Klein, T. B. R. Castro, J. Silva, M. Sundaram, M. K. Ellingson, T. Mao, J. E. Oh, B. Israelow, T. Takahashi, M. Tokuyama, P. Lu, A. Venkataraman, A. Park, S. Mohanty, H. Wang, A. L. Wyllie, C. B. F. Vogels, R. Earnest, S. Lapidus, I. M. Ott, A. J. Moore, M. C. Muenker, J. B. Fournier, M. Campbell, C. D. Odio, A. Casanovas-Massana, A. Obaid, A. Lu-Culligan, A. Nelson, A. Brito, A. Nunez, A. Martin, A. Watkins, B. Geng, C. Kalinich, C. Harden, C. Todeasa, C. Jensen, D. Kim, D. McDonald, D. Shepard, E. Courchaine, E. B. White, E. Song, E. Silva, E. Kudo, G. DeIuliis, H. Rahming, H.-J. Park, I. Matos, J. Nouws, J. Valdez, J. Fauver, J. Lim, K.-A. Rose, K. Anastasio, K. Brower, L. Glick, L. Sharma, L. Sewanan, L. Knaggs, M. Minasyan, M. Batsu, M. Petrone, M. Kuang, M. Nakahata, M. Campbell, M. Linehan, M. H. Askenase, M. Simonov, M. Smolgovsky, N. Sonnert, N. Naushad, P. Vijayakumar, R. Martinello, R. Datta, R. Handoko, S. Bermejo, S. Prophet, S. Bickerton, S. Velazquez, T. Alpert, T. Rice, W. Khoury-Hanold, X. Peng, Y. Yang, Y. Cao, Y. Strong, R. Herbst, A. C. Shaw, R. Medzhitov, W. L. Schulz, N. D. Grubaugh, C. D. Cruz, S. Farhadian, A. I. Ko, S. B. Omer, A. Iwasaki, Longitudinal analyses reveal immunological misfiring in severe COVID-19. *Nature*. **584**, 463–469 (2020).

6. J. Schulte-Schrepping, N. Reusch, D. Paclik, K. Baßler, S. Schlickeiser, B. Zhang, B. Krämer, T. Krammer, S. Brumhard, L. Bonaguro, E. D. Domenico, D. Wendisch, M. Grasshoff, T. S. Kapellos, M. Beckstette, T. Pecht, A. Saglam, O. Dietrich, H. E. Mei, A. R. Schulz, C. Conrad, D. Kunkel, E. Vafadarnejad, C.-J. Xu, A. Horne, M. Herbert, A. Drews, C. Thibeault, M. Pfeiffer, S. Hippenstiel, A. Hocke, H. Müller-Redetzky, K.-M. Heim, F. Machleidt, A. Uhrig, L. B. de Jarcy, L. Jürgens, M. Stegemann, C. R. Glösenkamp, H.-D. Volk, C. Goffinet, M. Landthaler, E. Wyler, P. Georg, M. Schneider, C. Dang-Heine, N. Neuwinger, K. Kappert, R. Tauber, V. Corman, J. Raabe, K. M. Kaiser, M. T. Vinh, G. Rieke, C. Meisel, T. Ulas, M. Becker, R. Geffers, M. Witzenrath, C. Drosten, N. Suttorp, C. von Kalle, F. Kurth, K. Händler, J. L. Schultze, A. C. Aschenbrenner, Y. Li, J. Nattermann, B. Sawitzki, A.-E. Saliba, L. E. Sander, D. C.-19 O. I. (DeCOI), A. Angelov, R. Bals, A. Bartholomäus, A. Becker, D. Bezdan, E. Bonifacio, P. Bork, T. Clavel, M. Colome-Tatche, A. Diefenbach, A. Dilthey, N. Fischer, K. Förstner, J.-S. Frick, J. Gagneur, A. Goesmann, T. Hain, M. Hummel, S. Janssen, J. Kalinowski, R. Kallies, B. Kehr, A. Keller, S. Kim-Hellmuth, C. Klein, O. Kohlbacher, J. O. Korbel, I. Kurth, M. Landthaler, Y. Li, K. Ludwig, O. Makarewicz, M. Marz, A. McHardy, C. Mertes, M. Nöthen, P. Nürnberg, U. Ohler, S. Ossowski, J. Overmann, S. Peter, K. Pfeffer, A. R. Poetsch, A. Pühler, N. Rajewsky, M. Ralser, O. Rieß, S. Ripke, U. N. da Rocha, P. Rosenstiel, A.-E. Saliba, L. E. Sander, B. Sawitzki, P. Schiffer, E.-C. Schulte, J. L. Schultze, A. Sczyrba, O. Stegle, J. Stoye, F. Theis, J. Vehreschild, J. Vogel, M. von Kleist, A. Walker, J. Walter, D. Wieczorek, J. Ziebuhr, Severe COVID-19 Is Marked by a Dysregulated Myeloid Cell Compartment. *Cell*. **182**, 1419-1440.e23 (2020).

7. T. S. Rodrigues, K. S. G. de Sá, A. Y. Ishimoto, A. Becerra, S. Oliveira, L. Almeida, A. V. Gonçalves, D. B. Perucello, W. A. Andrade, R. Castro, F. P. Veras, J. E. Toller-Kawahisa, D. C. Nascimento, M. H. F. de Lima, C. M. S. Silva, D. B. Caetite, R. B. Martins, I. A. Castro, M. C. Pontelli, F. C. de Barros, N. B. do Amaral, M. C. Giannini, L. P. Bonjorno, M. I. F. Lopes, R. C. Santana, F. C. Vilar, M. Auxiliadora-Martins, R. Luppino-Assad, S. C. L. de Almeida, F. R. de Oliveira, S. S. Batah, L. Siyuan, M. N. Benatti, T. M. Cunha, J. C. Alves-Filho, F. Q. Cunha, L. D. Cunha, F. G. Frantz, T. Kohlsdorf, A. T. Fabro, E. Arruda, R. D. R. de Oliveira, P. Louzada-Junior, D. S. Zamboni, Inflammasomes are activated in response to SARS-CoV-2 infection and

are associated with COVID-19 severity in patients. *J Exp Med*. **218** (2020), doi:10.1084/jem.20201707.

8. F. P. Veras, M. C. Pontelli, C. M. Silva, J. E. Toller-Kawahisa, M. de Lima, D. C. Nascimento, A. H. Schneider, D. Caetité, L. A. Tavares, I. M. Paiva, R. Rosales, D. Colón, R. Martins, I. A. Castro, G. M. Almeida, M. I. F. Lopes, M. N. Benatti, L. P. Bonjorno, M. C. Giannini, R. Luppino-Assad, S. L. Almeida, F. Vilar, R. Santana, V. R. Bollela, M. Auxiliadora-Martins, M. Borges, C. H. Miranda, A. Pazin-Filho, L. L. P. da Silva, L. Cunha, D. S. Zamboni, F. Dal-Pizzol, L. O. Leiria, L. Siyuan, S. Batah, A. Fabro, T. Mauad, M. Dolhnikoff, A. Duarte-Neto, P. Saldiva, T. M. Cunha, J. C. Alves-Filho, E. Arruda, P. Louzada-Junior, R. D. Oliveira, F. Q. Cunha, SARS-CoV-2–triggered neutrophil extracellular traps mediate COVID-19 pathology. *J Exp Med*. **217** (2020), doi:10.1084/jem.20201129.

9. R. Martins, A. R. Carlos, F. Braza, J. A. Thompson, P. Bastos-Amador, S. Ramos, M. P. Soares, Disease Tolerance as an Inherent Component of Immunity. *Annu Rev Immunol*. **37**, 405–437 (2019).

10. P. J. Murray, T. A. Wynn, Protective and pathogenic functions of macrophage subsets. *Nat Rev Immunol*. **11**, 723–737 (2011).

11. E. Boada-Romero, J. Martinez, B. Heckmann, D. Green, The clearance of dead cells by efferocytosis. *Nat Rev Mol Cell Bio*, 1–17 (2020).

12. L. Bosurgi, Y. G. Cao, M. Cabeza-Cabrerizo, A. Tucci, L. D. Hughes, Y. Kong, J. S. Weinstein, P. Licona-Limon, E. T. Schmid, F. Pelorosso, N. Gagliani, J. E. Craft, R. A. Flavell, S. Ghosh, C. V. Rothlin, Macrophage function in tissue repair and remodeling requires IL-4 or IL-13 with apoptotic cells. *Sci New York N Y*. **356**, 1072–1076 (2017).

13. N. A-Gonzalez, J. A. Quintana, S. García-Silva, M. Mazariegos, A. G. de la Aleja, J. A. A. Nicolás-Ávila, W. Walter, J. M. Adrover, G. Crainiciuc, V. K. Kuchroo, C. V. Rothlin, H. Peinado, A. Castrillo, M. Ricote, A. Hidalgo, Phagocytosis imprints heterogeneity in tissue-resident macrophages. *The Journal of experimental medicine*. **214**, 1281–1296 (2017).

14. J. S. A. Perry, S. Morioka, C. B. Medina, J. I. Etchegaray, B. Barron, M. H. Raymond, C. D. Lucas, S. Onengut-Gumuscu, E. Delpire, K. S. Ravichandran, Interpreting an apoptotic corpse as anti-inflammatory involves a chloride sensing pathway. *Nat Cell Biol*. **21**, 1532–1543 (2019).

15. C. V. Rothlin, T. D. Hille, S. Ghosh, Determining the effector response to cell death. *Nat Rev Immunol*, 1–13 (2020).

16. N. Zhu, W. Wang, Z. Liu, C. Liang, W. Wang, F. Ye, B. Huang, L. Zhao, H. Wang, W. Zhou, Y. Deng, L. Mao, C. Su, G. Qiang, T. Jiang, J. Zhao, G. Wu, J. Song, W. Tan, Morphogenesis and cytopathic effect of SARS-CoV-2 infection in human airway epithelial cells. *Nat Commun*. **11**, 3910 (2020).

17. H. Chu, J. F.-W. Chan, T. T.-T. Yuen, H. Shuai, S. Yuan, Y. Wang, B. Hu, C. C.-Y. Yip, J. O.-L. Tsang, X. Huang, Y. Chai, D. Yang, Y. Hou, K. K.-H. Chik, X. Zhang, A. Y.-F. Fung, H.-W. Tsoi, J.-P. Cai, W.-M. Chan, J. D. Ip, A. W.-H. Chu, J. Zhou, D. C. Lung, K.-H. Kok, K. K.-W. To, O. T.-Y. Tsang, K.-H. Chan, K.-Y. Yuen, Comparative tropism, replication kinetics, and cell damage profiling of SARS-CoV-2 and SARS-CoV with implications for clinical manifestations, transmissibility, and laboratory studies of COVID-19: an observational study. *Lancet Microbe*. **1**, e14–e23 (2020).

18. Y. Ren, T. Shu, D. Wu, J. Mu, C. Wang, M. Huang, Y. Han, X.-Y. Zhang, W. Zhou, Y. Qiu, X. Zhou, The ORF3a protein of SARS-CoV-2 induces apoptosis in cells. *Cell Mol Immunol*. **17**, 881–883 (2020).

19. V. A. Fadok, D. R. Voelker, P. A. Campbell, J. J. Cohen, D. L. Bratton, P. M. Henson, Exposure of phosphatidylserine on the surface of apoptotic lymphocytes triggers specific recognition and removal by macrophages. *J Immunol Baltim Md 1950*. **148**, 2207–16 (1992).

20. S. Nagata, Apoptosis and Clearance of Apoptotic Cells. *Annu Rev Immunol*. **36**, 489–517 (2018).

21. A. C. Doran, A. Yurdagul, I. Tabas, Efferocytosis in health and disease. *Nat Rev Immunol*. **20**, 254–267 (2020).

22. K. K. Penberthy, K. S. Ravichandran, Apoptotic cell recognition receptors and scavenger receptors. *Immunological reviews*. **269**, 44–59 (2016).

23. D. Park, C. Z. Han, M. R. Elliott, J. M. Kinchen, P. C. Trampont, S. Das, S. Collins, J. J. Lysiak, K. L. Hoehn, K. S. Ravichandran, Continued clearance of apoptotic cells critically depends on the phagocyte Ucp2 protein. *Nature*. **477**, 220–4 (2011).

24. S. Morioka, J. S. A. Perry, M. H. Raymond, C. B. Medina, Y. Zhu, L. Zhao, V. Serbulea, S. Onengut-Gumuscu, N. Leitinger, S. Kucenas, J. C. Rathmell, L. Makowski, K. S. Ravichandran, Efferocytosis induces a novel SLC program to promote glucose uptake and lactate release. *Nature*. **563**, 714–718 (2018).

25. A. Yurdagul, M. Subramanian, X. Wang, S. B. Crown, O. R. Ilkayeva, L. Darville, G. K. Kolluru, C. C. Rymond, B. D. Gerlach, Z. Zheng, G. Kuriakose, C. G. Kevil, J. M. Koomen, J. L. Cleveland, D. M. Muoio, I. Tabas, Macrophage Metabolism of Apoptotic Cell-Derived Arginine Promotes Continual Efferocytosis and Resolution of Injury. *Cell Metab*. **31**, 518-533.e10 (2020).

26. M. Miyanishi, K. Tada, M. Koike, Y. Uchiyama, T. Kitamura, S. Nagata, Identification of Tim4 as a phosphatidylserine receptor. *Nature*. **450**, 435–439 (2007).

27. Y. Wang, M. Subramanian, A. Yurdagul, V. C. Barbosa-Lorenzi, B. Cai, J. de Juan-Sanz, T. A. Ryan, M. Nomura, F. R. Maxfield, I. Tabas, Mitochondrial Fission Promotes the Continued Clearance of Apoptotic Cells by Macrophages. *Cell*. **171**, 331-345.e22 (2017).

28. A. A. J. Hamers, H. Q. Dinh, G. D. Thomas, P. Marcovecchio, A. Blatchley, C. S. Nakao, C. Kim, C. McSkimming, A. M. Taylor, A. T. Nguyen, C. A. McNamara, C. C. Hedrick, Human Monocyte Heterogeneity as Revealed by High-Dimensional Mass Cytometry. *Arteriosclerosis Thrombosis Vasc Biology*. **39**, 25–36 (2019).

29. J. F. Tait, C. Smith, Phosphatidylserine Receptors: Role of CD36 in Binding of Anionic Phospholipid Vesicles to Monocytic Cells*. *J Biol Chem*. **274**, 3048–3054 (1999).

30. B. W. Parks, L. L. Black, K. A. Zimmerman, A. E. Metz, C. Steele, J. E. Murphy-Ullrich, J. H. Kabarowski, CD36, but not G2A, modulates efferocytosis, inflammation, and fibrosis following bleomycin-induced lung injury[S]. *J Lipid Res*. **54**, 1114–1123 (2013).

31. B. J. Webb, I. D. Peltan, P. Jensen, D. Hoda, B. Hunter, A. Silver, N. Starr, W. Buckel, N. Grisel, E. Hummel, G. Snow, D. Morris, E. Stenehjem, R. Srivastava, S. M. Brown, Clinical criteria for COVID-19-associated hyperinflammatory syndrome: a cohort study. *Lancet Rheumatology* (2020), doi:10.1016/s2665-9913(20)30343-x.

32. M. Liao, Y. Liu, J. Yuan, Y. Wen, G. Xu, J. Zhao, L. Cheng, J. Li, X. Wang, F. Wang, L. Liu, I. Amit, S. Zhang, Z. Zhang, Single-cell landscape of bronchoalveolar immune cells in patients with COVID-19. *Nat Med*. **26**, 842–844 (2020).

33. A. M. Jamieson, L. Pasman, S. Yu, P. Gamradt, R. J. Homer, T. Decker, R. Medzhitov, Role of Tissue Protection in Lethal Respiratory Viral-Bacterial Coinfection. *Science*. **340**, 1230–1234 (2013).

34. L. Chen, X. Long, Q. Xu, J. Tan, G. Wang, Y. Cao, J. Wei, H. Luo, H. Zhu, L. Huang, F. Meng, L. Huang, N. Wang, X. Zhou, L. Zhao, X. Chen, Z. Mao, C. Chen, Z. Li, Z. Sun, J. Zhao, D. Wang, G. Huang, W. Wang, J. Zhou, Elevated serum levels of S100A8/A9 and HMGB1 at hospital admission are correlated with inferior clinical outcomes in COVID-19 patients. *Cell Mol Immunol*. **17**, 992–994 (2020).

35. Y. Han, H. Zhang, S. Mu, W. Wei, C. Jin, Y. Xue, C. Tong, Y. Zha, Z. Song, G. Gu, *Medrxiv*, in press, doi:10.1101/2020.03.24.20040162.

36. P. Bastard, L. B. Rosen, Q. Zhang, E. Michailidis, H.-H. Hoffmann, Y. Zhang, K. Dorgham, Q. Philippot, J. Rosain, V. Béziat, J. Manry, E. Shaw, L. Haljasmägi, P. Peterson, L. Lorenzo, L. Bizien, S. Trouillet-Assant, K. Dobbs, A. A. de Jesus, A. Belot, A. Kallaste, E. Catherinot, Y. Tandjaoui-Lambiotte, J. L. Pen, G. Kerner, B. Bigio, Y. Seeleuthner, R. Yang, A. Bolze, A. N. Spaan, O. M. Delmonte, M. S. Abers, A. Aiuti, G. Casari, V. Lampasona, L. Piemonti, F. Ciceri, K. Bilguvar, R. P. Lifton, M. Vasse, D. M. Smadja, M. Migaud, J. Hadjadj, B. Terrier, D. Duffy, L. Quintana-Murci, D. van de Beek, L. Roussel, D. C. Vinh, S. G. Tangye, F. Haerynck, D. Dalmau, J. Martinez-Picado, P. Brodin, M. C. Nussenzweig, S. Boisson-Dupuis, C. Rodríguez-Gallego, G. Vogt, T. H. Mogensen, A. J. Oler, J. Gu, P. D. Burbelo, J. Cohen, A. Biondi, L. R. Bettini, M. D'Angio, P. Bonfanti, P. Rossignol, J. Mayaux, F. Rieux-Laucat, E. S. Husebye, F. Fusco, M. V. Ursini, L. Imberti, A. Sottini, S. Paghera, E. Quiros-Roldan, C. Rossi, R. Castagnoli, D. Montagna, A. Licari, G. L. Marseglia, X. Duval, J. Ghosn, H. Lab§, N.-U. I. R. to

C. Group§, C. Clinicians§, C.-S. Clinicians§, I. C. Group§, F. C. C. S. Group§, T. M. I. Consortium§, C.-C. Cohort§, A. U. C.-19 Biobank§, C. H. G. Effort§, J. S. Tsang, R. Goldbach-Mansky, K. Kisand, M. S. Lionakis, A. Puel, S.-Y. Zhang, S. M. Holland, G. Gorochov, E. Jouanguy, C. M. Rice, A. Cobat, L. D. Notarangelo, L. Abel, H. C. Su, J.-L. Casanova, Auto-antibodies against type I IFNs in patients with life-threatening COVID-19. *Science*, eabd4585 (2020).

37. Y. Zuo, S. K. Estes, R. A. Ali, A. A. Gandhi, S. Yalavarthi, H. Shi, G. Sule, K. Gockman, J. A. Madison, M. Zuo, V. Yadav, J. Wang, W. Woodard, S. P. Lezak, N. L. Lugogo, S. A. Smith, J. H. Morrissey, Y. Kanthi, J. S. Knight, Prothrombotic autoantibodies in serum from patients hospitalized with COVID-19. *Sci Transl Med*. **12**, eabd3876 (2020).

38. M. Zuniga, C. Gomes, S. E. Carsons, M. T. Bender, P. Cotzia, Q. R. Miao, D. C. Lee, A. Rodriguez, Autoimmunity to the Lung Protective Phospholipid-Binding Protein Annexin A2 Predicts Mortality Among Hospitalized COVID-19 Patients, doi:10.1101/2020.12.28.20248807.

39. J. Martinez, L. D. Cunha, S. Park, M. Yang, Q. Lu, R. Orchard, Q.-Z. Li, M. Yan, L. Janke, C. Guy, A. Linkermann, H. W. Virgin, D. R. Green, Noncanonical autophagy inhibits the autoinflammatory, lupus-like response to dying cells. *Nature*. **533**, 115–9 (2016).

40. P. L. Cohen, R. Caricchio, V. Abraham, T. D. Camenisch, J. C. Jennette, R. A. S. Roubey, H. S. Earp, G. Matsushima, E. A. Reap, Delayed Apoptotic Cell Clearance and Lupus-like Autoimmunity in Mice Lacking the c-mer Membrane Tyrosine Kinase. *J Exp Medicine*. **196**, 135–140 (2002).

41. Y. Peng, K. B. Elkon, Autoimmunity in MFG-E8–deficient mice is associated with altered trafficking and enhanced cross-presentation of apoptotic cell antigens. *J Clin Invest*. **121**, 2221–2241 (2011).

42. R. Rodriguez-Manzanet, M. A. Sanjuan, H. Y. Wu, F. J. Quintana, S. Xiao, A. C. Anderson, H. L. Weiner, D. R. Green, V. K. Kuchroo, T and B cell hyperactivity and autoimmunity associated with niche-specific defects in apoptotic body clearance in TIM-4-deficient mice. *P Natl Acad Sci Usa*. **107**, 8706–11 (2010).

43. V. M. Corman, O. Landt, M. Kaiser, R. Molenkamp, A. Meijer, D. K. Chu, T. Bleicker, S. Brünink, J. Schneider, M. L. Schmidt, D. G. Mulders, B. L. Haagmans, B. van der Veer, S. van den Brink, L. Wijsman, G. Goderski, J.-L. Romette, J. Ellis, M. Zambon, M. Peiris, H. Goossens, C. Reusken, M. P. Koopmans, C. Drosten, Detection of 2019 novel coronavirus (2019-nCoV) by real-time RT-PCR. *Eurosurveillance*. **25**, 2000045 (2020).

44. L. J. Reed, H. Muench, A simple method of estimating fifty per cent endpoints. *Am J Epidemiol*. **27**, 493–497 (1938).

Acknowledgements

The authors thank Lais M. R. Cantano, Denise M. da Fonseca, Elizabete R. Milani and Roberta R. C. Rosales (FMRP-USP) for technical assistance and Jennifer Martinez (NIEHS, NIH) for thoughtful insights and discussions. This work was supported by grants from the Fundo de Amparo a Pesquisa do Estado de São Paulo - FAPESP (2018/25559-4 and 2020/05288-6), Coordenação de Aperfeiçoamento de Pessoal de Nível Superior - CAPES (88887.507253/2020-00) and Conselho Nacional de Desenvolvimento Científico e Tecnológico – CNPq (434538/2018-3). D.S., A. C. G. S., T. S. R. are supported by FAPESP fellowships.

Author Contributions

D. S., A. C. G. S., T. S. R., and L.D.C. designed the experiments; D. S., A. C. G. S. and T. S. R. performed and analyzed the experiments; M. F. R., E. G. F. F., D. L. A. T., M. H. F. L., D. B. C. N., and I. C. performed and analyzed specific experiments; C. M. S., J. E. T., A. B., S. O., D. B. C., L. A., A. Y. I., T. M. L., R. B. M., F. V., N. B. A., M. C. G., L. P. B., M I. F. L., M. N. B., R. C. S., F. C. V., M. A. M., R. L. A., S. C. L. A and F. R. O. provided resources and/or analysis of clinical data. E. A., T. M. C., J. C. A. F., A. F., H. N., D. S. Z. provided resources and discussed original data. P. L. J. and R. D. R. O. provided resources, analyzed clinical data, and discussed original data. L. D. C. provided funds and supervised the project. D. S., A. C. G. S., T. S. R., and L. D. C. wrote the manuscript and all other authors revised the original draft.

Competing Interests

The authors declare no competing financial interests.

Data Availability

All data are available in the main text or the supplementary materials.

Figures and Tables

Fig. 1. Macrophages engulf dying cells carrying viable SARS-CoV-2.

(A) Percentage of annexin V^+ in Vero CCL81 and Calu-3 cells UV-irradiated (UV-AC) for induction of apoptosis or infected with SARS-CoV-2 (Cov2-AC) for 48h, as assessed by flow cytometry analysis.

(B-C) Analysis of intracellular cleaved caspase-3 on Vero CCL81 infected with SARS-CoV-2 for 48h in the absence (DMSO) or presence of pan-caspase inhibitor zVAD-FMK (20 μM). Frequency of cleaved Casp-3^+ cells (B) and geometric mean fluorescence intensity (MFI) (C, expressed as fold change relative to Cntrl) were assessed by flow cytometry.

(D-E) Representative histograms (D) and frequency (E) of $Spike^+$ permeabilized apoptotic Vero CCL81 (CoV2-Vero, green) and Calu-3 (CoV2-Calu, blue), infected with SARS-CoV-2 for 48h. The frequency of Spike-positive cells was estimated using UV-irradiated cells (dark yellow) as negative controls.

(F-G) $TCID_{50}$ quantification of SARS-CoV-2 viral loads in apoptotic cells (CoV2-AC) and their supernatant (CoV2-AC Sup) 48h post-infection, for Vero CCL81 (F) and Calu-3 (G) cells.

(H-J) Representative plot (H) and percentage for the engulfment of UV-AC and CoV2-AC $CFSE^+$ apoptotic Vero CCL81 (I) and Calu-3 cells (J) by THP-1-derived macrophages (gated on Single cells/Live cells/Cell Trace $FarRed^+$), determined by flow cytometry.

(K) Representative maximal projection of scanning confocal images of Spike immunostaining (anti-Spike, red) in THP-1-derived macrophages fed with UV-AC or CoV2-AC (from Vero CCL81, CFSE-labelled, green). Cell nuclei were stained with Hoechst (blue). Scale bar: 10 µm.

(L) Frequency of THP-1-derived macrophages untreated (Cntrl) or stimulated with UV-AC; CoV2-AC, CoV2-AC Sup or SARS-CoV-2 infection at MOI of 1 (CoV2). Macrophages were stained with a viability probe (Zombie Violet) 24h post-stimulation and analyzed by flow cytometry.

(A-L) Each data point is from an independent sample. Bar represents mean ± S.E.M. Significance was calculated by ANOVA (B, C, L) or Student's test (E-J). *p<0.05

Fig. 2. Engulfment of SARS-CoV-2-infected dying cells impairs macrophage anti-inflammatory functions.

(A) *MRC1* (*CD206*) expression in THP1-derived macrophages untreated (Cntrl), stimulated with UV-irradiated (UV-AC), SARS-CoV-2-infected (CoV2-AC) or the culture supernatant of infected (CoV2-AC Sup) apoptotic Vero CCL81 cells, or infected with CoV2 at MOI of 1 (CoV2). mRNA expression was determined by RT-qPCR and normalized to *GAPDH.*

(B-C) Flow cytometric analysis of CD206 expression on the cell surface of THP1-derived macrophages stimulated with UV-AC, CoV2-AC or CoV2-AC Sup obtained from Vero CCL81 cells. Representative histogram (B) and quantification of geometric mean fluorescence intensity (MFI), shown as fold change relative to Cntrl (C).

(D) Flow cytometric analysis of CD206 expression on the cell surface of THP1-derived macrophages stimulated with CoV2-AC or CoV2-AC Sup from Vero CCL81, treated or not with

UV-irradiation before stimulation, as indicated. Non-infected, UV-irradiated Vero cells (UV-AC) were used as positive control. Data represents the fold change of MFI relative to Cntrl.

(E) Flow cytometric analysis of CD206 expression on the cell surface of THP1-derived macrophages stimulated with CoV2-AC, CoV2-AC Sup or infected with CoV2 in the presence of UV-irradiated apoptotic bodies (UV-AC + CoV2), as assessed by flow cytometry. Data are expressed as fold change of MFI relative to Cntrl.

(F) *IL6* expression in THP1-derived macrophages untreated (Cntrl), stimulated with UV-irradiated (UV-AC), SARS-CoV-2-infected (CoV2-AC), or the culture supernatant of infected (CoV2-AC Sup) apoptotic Vero CCL81 cells, or infected with CoV2 at MOI 1 (CoV2). mRNA expression was determined by RT-qPCR and normalized to *GAPDH.*

(G-I) CBA quantification of IL-6 in the culture supernatants of macrophages (Mϕ) stimulated for 24h with UV-AC, CoV2-AC or CoV2-AC Sup obtained from Vero CCL81 or Calu-3 cells, as indicated.

(J-L) CBA quantification of IL-1β in the culture supernatants of macrophages (Mϕ) stimulated for 24h with UV-AC, CoV2-AC or CoV2-AC Sup obtained from Vero CCL81 or Calu-3 cells, as indicated.

(M) ELISA quantification of IL-6 in the culture supernatants of THP1-derived macrophages stimulated with CoV2-AC obtained from Vero CCL81 cells, treated or not with UV-irradiation (UV) or fixed with 2% paraformaldehyde (Fix) before stimulation. Non-infected, UV-irradiated Vero cells (UV-AC) were used as negative control.

(A-M) Each data point is from an independent sample. Bar represents mean ± S.E.M. Significance was calculated by ANOVA test. *$p<0.05$

Fig. 3. Engulfment of SARS-CoV-2-infected dying cells suppresses continual efferocytosis by macrophages.

(A-E) mRNA expression of *CD36* (A), *SRA-I* (B), *ITGB5* (C), *TIMD4* (D), and *MERTK* (E), determined by RT-qPCR and normalized to *GAPDH*, in THP1-derived macrophages untreated (Cntrl), stimulated with UV-irradiated (UV-AC), SARS-CoV-2-infected (CoV2-AC) or the culture supernatant of infected (CoV2-AC Sup) apoptotic Vero CCL81 cells, or infected with CoV2 at MOI 1 (CoV2).

(F) Percentage of THP1-derived macrophages engulfing UV-AC in a two-step efferocytosis assay by flow cytometry. Engulfment of Cell Trace FarRed^{+} UV-AC were tracked in CellTrace Violet $^{+}$ macrophages stimulated in a first-round with PhRODO^{+} UV-AC or CoV2-AC (gated on Single cells/Live cells/ CellTrace Violet $^{+}$/PhRODO^{+}).

(G) Percentage of THP1-derived macrophages engulfing UV-AC in a one-step efferocytosis assay by flow cytometry. Engulfment of Cell Trace FarRed^{+} UV-AC were tracked in CellTrace Violet $^{+}$ macrophages untreated or infected at MOI of 1 (CoV2) (gated on Single cells/Live cells/ CellTrace Violet $^{+}$).

(A-G) Each data point is from an independent sample. Bar represents mean ± S.E.M. Significance was calculated by ANOVA (A-E) or Student's test (F, G). *p<0.05

Fig. 4. Efferocytosis is impaired in monocytes from COVID-19 patients.

(A-C) Frequency of classical CD14^{+}CD16^{-} (A), intermediate CD14^{hi}CD16^{+} (B) and non-classical CD14^{int}CD16^{+} (C) monocytes in blood samples from healthy donors (HC) and COVID-19 patients, determined by flow cytometry (pre-gated on Single cells/Live cells/Lin^{-} CD14^{+}).

(D-F) Representative dot plots (D), frequency (E), and MFI (F) of CD36 expression on the surface of monocytes (pre-gated on Single cells/Live cells/Lin$^-$ CD14$^+$) in blood samples from healthy donors (HC) and COVID-19 patients.

(**G-K**) mRNA expression of *CD36* (G), *SRA-I* (H), *ITGB5* (I), *TIMD4* (J), and *MERTK* (K) determined by RT-qPCR and normalized to *GAPDH*, in PBMCs from healthy donors (HC) and COVID-19 patients.

(L-N) Stratification of *CD36* (L), *SRA*-1 (M), and *TIMD4* (N) expression according to patients' cHIS score.

(O) Representative scanning confocal images of monocytes from healthy donors (HC) and COVID-19 patients stimulated with UV-irradiated apoptotic murine thymocytes for 1h. The actin filaments (F-actin) were stained with phalloidin (AF-488, green) and the nuclei were stained with Hoescht (blue). White arrows point to engulfed thymocytes. Scale bar: 10 μm.

(**P-Q**) Percentage of monocytes of healthy donors (HC) and COVID-19 patients engulfing apoptotic thymocytes (P) or zymosan (Q), determined by epifluorescence microscopy (as described in (O)).

(A-K) Each data point is from an independent sample. The crossing line represents mean and error bars ± S.E.M. Significance was calculated by Mann-Whitney test. *p<0.05.

Fig. 5. Lung-infiltrating monocytes and macrophages of COVID-19 patients express lower levels of efferocytic receptors.

(A) Heatmap showing log2 fold change in the expression of genes, in cells obtained from the bronchoalveolar lavage of mild and severe COVID-19 patients versus healthy individuals,

comprising early-infiltrating phagocytes (S1009^{+} CCL18^{-}) and in anti-inflammatory monocytes-derived macrophages (CD14^{+} S11009^{-} CCL18^{+}) clusters.

(B-E) Immunofluorescence histological analysis in autopsied post-mortem lung tissues from control (CT) and COVID-19 patients. Tissue samples were immunolabelled with anti-CD36 (B and C, red), anti-MERTK (D and E, red), and anti-S1009 (green) and stained with DAPI (blue). (B and D) Representative images show cropped details of lung tissues scanned by wide-field epifluorescence imaging. Scale bar: 10 μm. The MFI of CD36 (C) and MERTK (E) of at least 200 S1009^{+} cells were determined (n = 3 individuals per group). Each data point represents a S1009+ cell. The crossing line represents mean and error bars ± S.E.M. Significance was calculated by Student's t-test. *p<0.05.

Supplementary Materials

Fig. S1. **Engulfment of SARS-CoV-2-infected dying cells switches macrophage phenotype in response to efferocytosis.**

(A-B) Flow cytometric analysis of CD206 expression on the cell surface of THP1-derived macrophages stimulated with UV-AC, CoV2-AC or CoV2-AC Sup obtained from Calu-3 cells. Representative histogram (A) and quantification of MFI, shown as fold change relative to Cntrl (B).

(C-D) Flow cytometric analysis of CD206 expression on the cell surface of PBMC-derived macrophages stimulated with UV-AC, CoV2-AC or CoV2-AC Sup obtained from Vero CCL81 cells. Representative histogram (C) and quantification of geometric mean fluorescence intensity (MFI), shown as fold change relative to Cntrl (D).

(E-F) *MRC1* (*CD206*) (E) and IL-6 (F) expression in PBMC-derived macrophages untreated (Cntrl) or stimulated with SARS-CoV-2-infected (CoV2-AC) apoptotic Vero CCL81 cells. mRNA expression was determined by RT-qPCR and normalized to *GAPDH*.

(A-F) Each data point is from an independent sample. Bar represents mean ± S.E.M. Significance was calculated by ANOVA test (B, D) or Student's t-test (E, F). or *$p<0.05$

Fig. S2. **Analysis of cytokine production and monocyte populations in COVID-19 patients**.

(A-F) The levels of the IL-6 (A), IL-8 (B), IL-10 (C), IL-1β (D), TNF-α (E) and IL-12 (F) were measured in plasma from healthy donors (HC) and COVID-19 patients. Data are expressed as the individual data points showing median bar and interquartile range and were quantified by flow cytometry using CBA. Significance was calculated by the Mann-Whitney test. *$p<0.05$.

(G) Representative plots for the gating strategy used in Figs. 5A-F and Fig. S2H-J.

(H-I) Frequency (H) and the absolute number (I) of $CD14^+$ monocytes in the blood from healthy donors (HC) and COVID-19 patients, determined by flow cytometry (gated on Single cells/Live cells/Lin^-). Each data point is from an independent sample. The crossing line represents mean and error bars ± S.E.M. Significance was calculated by Mann-Whitney test. *$p<0.05$.

(J) Percentage of HLA-DR^+ monocytes in blood from healthy donors (HC) and COVID-19 patients, determined by flow cytometry (gated on Single cells/Live cells/Lin^- $CD14^+$). Each data point is from an independent sample. The crossing line represents mean and error bars ± S.E.M. Significance was calculated by Mann-Whitney test. *$p<0.05$.

Table S1. COVID-19 patients medical characteristics.

A
% of AnnexinV+
UV-AC
CoV2-AC
Vero Calu-3

B
Cleaved Casp-3+ (%)
ns
Cntrl
CoV2-AC
DMSO zVAD

C
Cleaved Casp-3 MFI (fold)
ns
Cntrl
CoV2-AC
DMSO zVAD

D
Vero Calu-3
Cntrl CoV2-Vero CoV2-Calu
Spike-AF647

E
Spike+ (%)
CoV2-Vero
CoV2-Calu

F
Vero
Log_{10} $TCID_{50}$/mL
ns

G
Calu-3
Log_{10} $TCID_{50}$/mL
ns
CoV2-AC
CoV2-AC Sup

H
UV-AC CoV2-AC
Vero
20.2% 51.8%
Calu-3
23.5% 37.8%
Cell Trace FarRed
CFSE

I
Vero
Engulfment (%CFSE+)

J
Calu-3
Engulfment (%CFSE+)
UV-AC
CoV2-AC

K
HOECHST CFSE Spike Merge DIC
UV-AC
CoV2-AC

L
Viability (%)
Cntrl
UV-AC
CoV2-AC
CoV2- AC Sup
CoV2

Figure 2. **dos-Santos, Salina, Rodrigues *et al.***

A

MRC1

Fold change (relative to cntrl)

6.0 4.5 3.0 1.5 0.0

*

Cntrl
UV-AC
CoV2-AC
CoV2 + AC Sup
CoV2

B

Vero

CD206-FITC

C

CD206 MFI (fold)

8 6 4 2 0

*

Cntrl
UV-AC
CoV2-AC
CoV2 + AC Sup

D

CD206 MFI (fold)

40 30 20 10 0

*
*

UV

Cntrl
UV-AC
CoV2-AC
CoV2-AC Sup

E

CD206 MFI (fold)

8 6 4 2 0

*
ns
*
*

Cntrl
UV-AC
CoV2-AC
UV-AC + CoV2
CoV2

F

IL6

Fold change (relative to cntrl)

8000 6000 4000 2000 0

*
*

Cntrl
UV-AC
CoV2-AC
CoV2-AC Sup
CoV2

G

THP1-Mϕ +Vero

IL-6 (ng/mL)

32 24 16 8 0

*

H

THP1-Mϕ + Calu-3

IL-6 (ng/mL)

32 24 16 8 0

*

I

PBMC-Mϕ +Vero

IL-6 (ng/mL)

4 3 2 1 0

*

Cntrl
UV-AC
CoV2-AC
CoV2-AC Sup

J

THP1-Mϕ + Vero

IL-1β (ng/mL)

20 15 10 5 0

*

K

THP1-Mϕ + Calu-3

IL-1β (ng/mL)

20 15 10 5 0

*

L

PBMC-Mϕ + Vero

IL-1β (ng/mL)

0.15 0.10 0.05 0.00

*

Cntrl
UV-AC
CoV2-AC
CoV2-AC Sup

M

IL-6 (ng/mL)

6.0 4.5 3.0 1.5 0.0

*

UV Fix

Cntrl
UV-AC
CoV2-AC

Figure 3. **dos-Santos, Salina, Rodrigues *et al.***

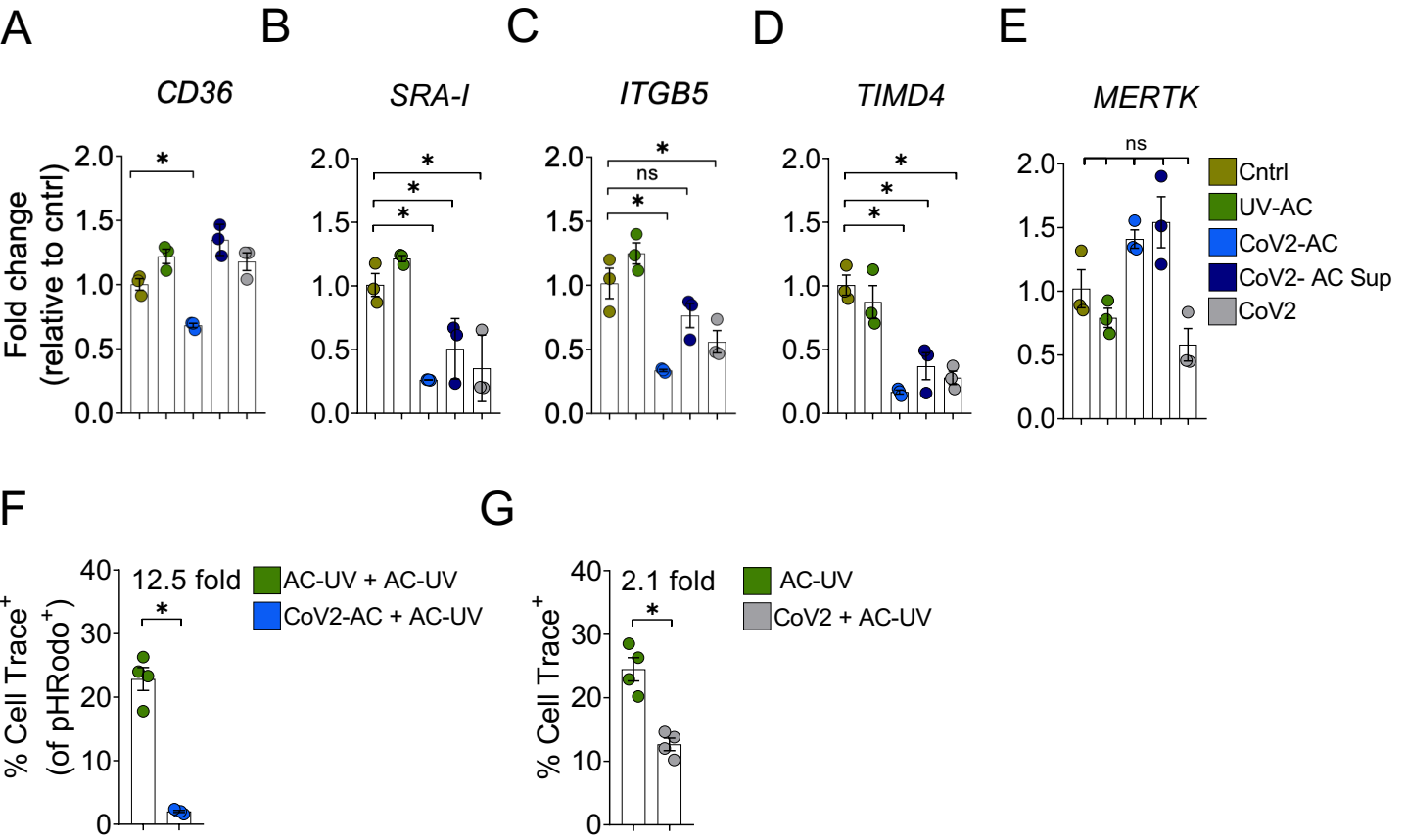

Figure 4. **dos-Santos, Salina, Rodrigues *et al.***

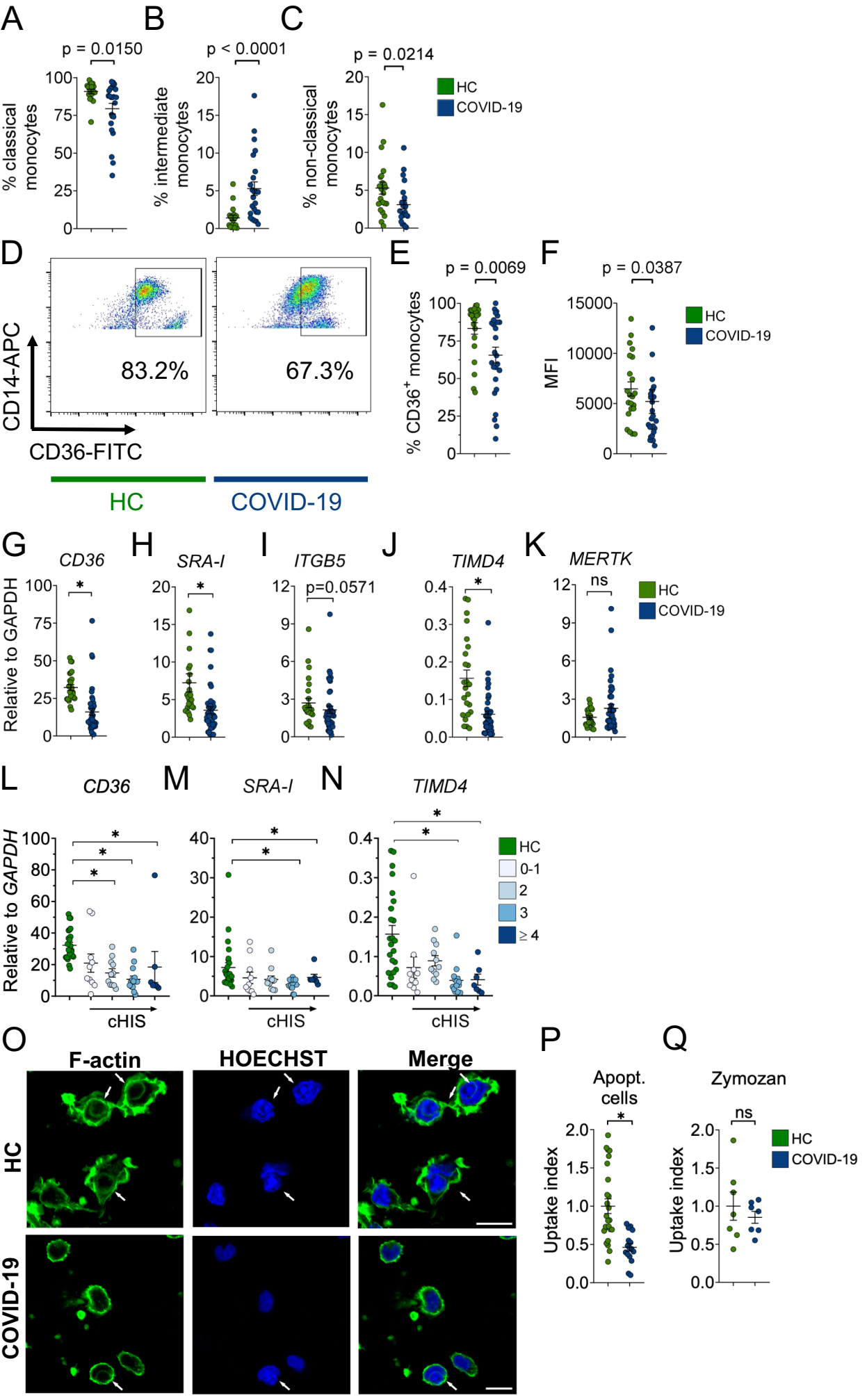

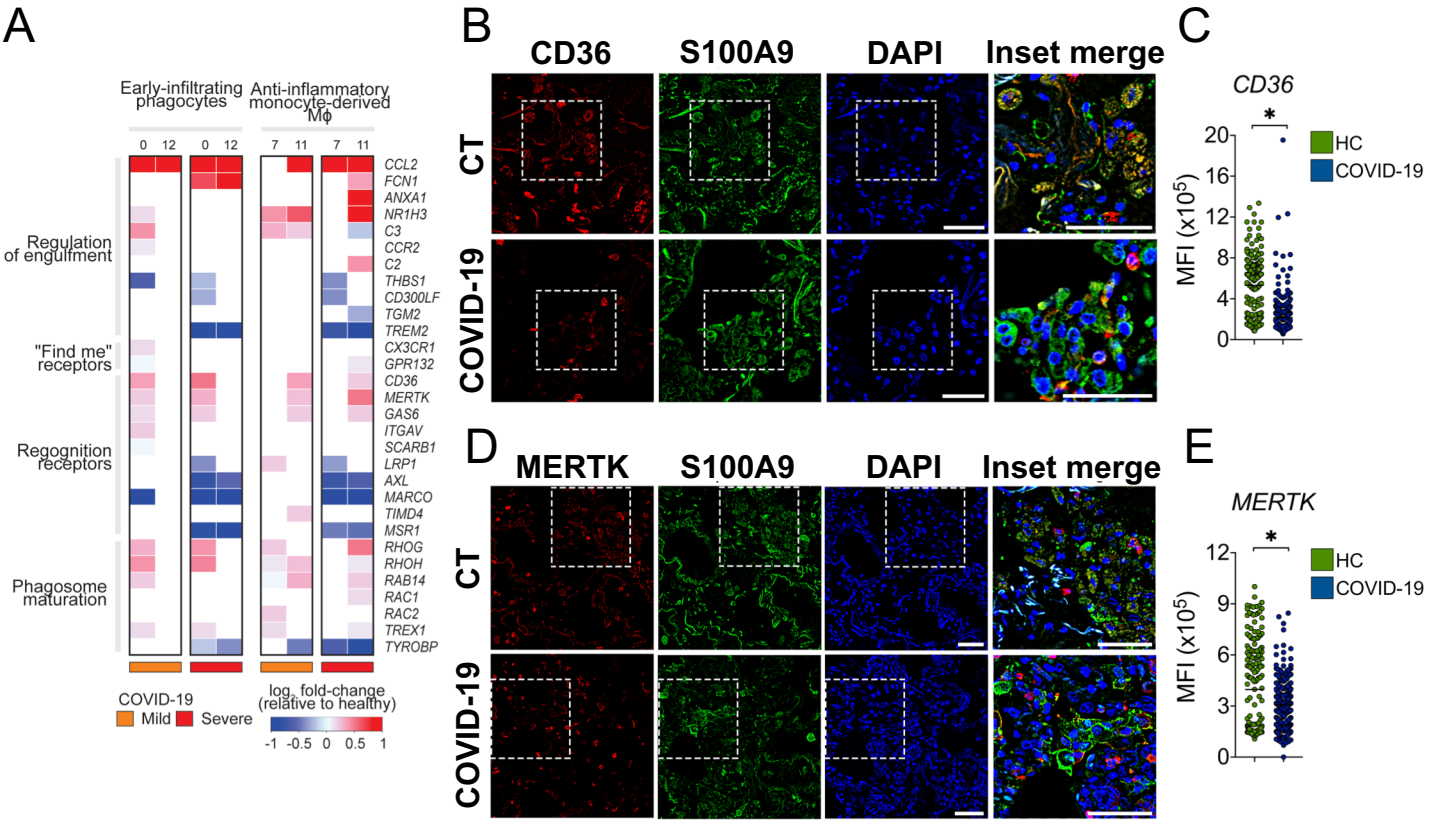
A
Early-infiltrating phagocytes
Anti-inflammatory monocyte-derived Mϕ
0 12 0 12 7 11 7 11
Regulation of engulfment
"Find me" receptors
Regognition receptors
Phagosome maturation
CCL2
FCN1
ANXA1
NR1H3
C3
CCR2
C2
THBS1
CD300LF
TGM2
TREM2
CX3CR1
GPR132
CD36
MERTK
GAS6
ITGAV
SCARB1
LRP1
AXL
MARCO
TIMD4
MSR1
RHOG
RHOH
RAB14
RAC1
RAC2
TREX1
TYROBP
COVID-19
Mild
Severe
log2 fold-change (relative to healthy)
-1 -0.5 0 0.5 1
B
CD36
S100A9
DAPI
Inset merge
CT
COVID-19
C
CD36
MFI (x10^5)
HC
COVID-19
D
MERTK
S100A9
DAPI
Inset merge
CT
COVID-19
E
MERTK
MFI (x10^5)
HC
COVID-19

Figure S1. **dos-Santos, Salina, Rodrigues *et al.***

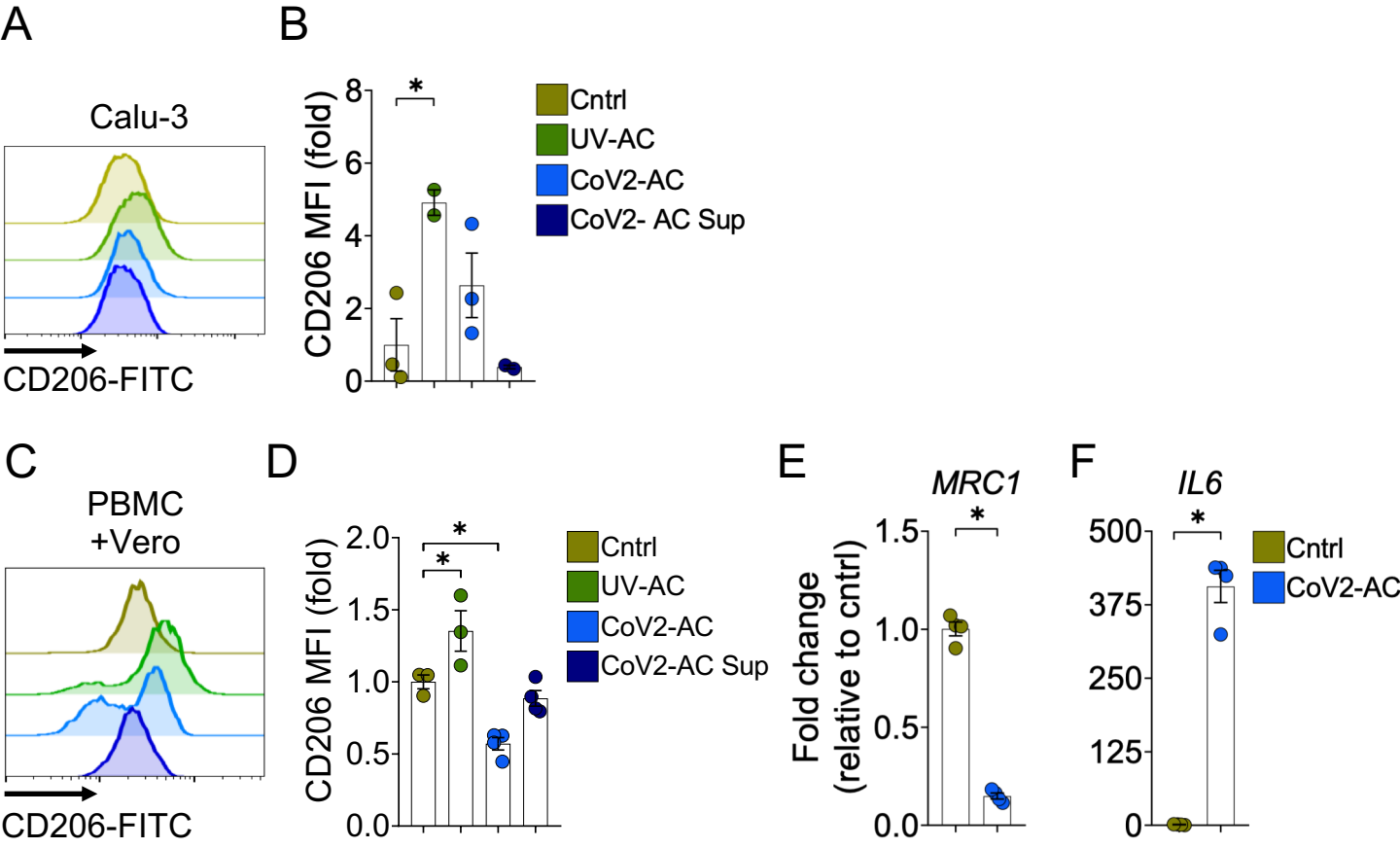

Figure S2. **dos-Santos, Salina, Rodrigues *et al.***

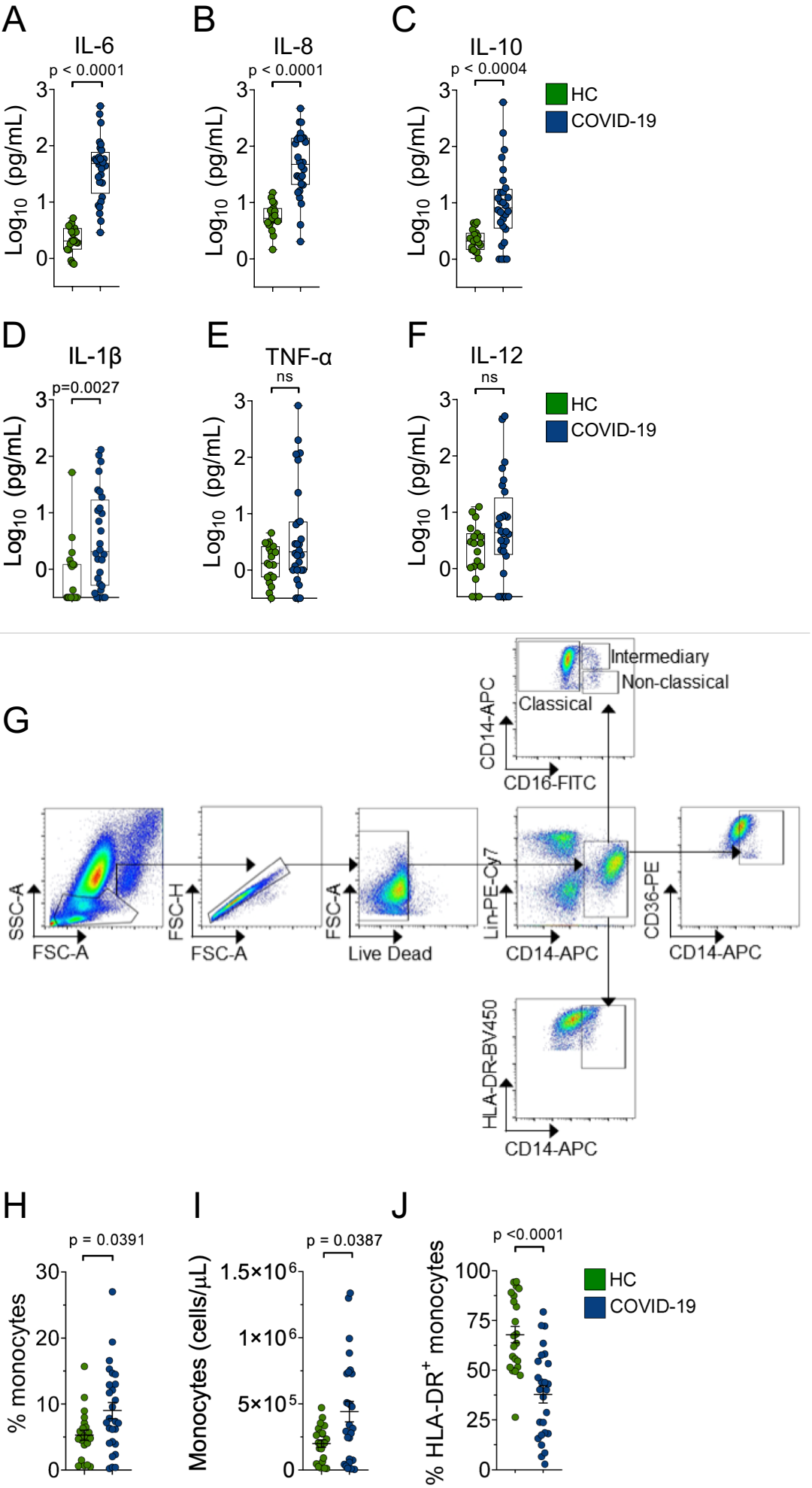

Table S1 - COVID-19 patients medical characteristics

Demographics		**%**
Number	59	
Age	61.58 ± 16.20	
Female		42.4
Comorbidities		
Hypertension	34	58
Obesity	31	56
Diabetes	21	36
History of smoking	8	15
Heart disease	15	26
Lung disease	11	19
Kidney disease	7	12
Cancer	6	10
History of stroke	1	2
Immunodeficiency	1	2
Autoimmune diseases	2	3
Laboratorial findings		
CRP (mg/dL)*	11.50 ± 7.97	
D-Dimers (µg/mL)**	3.25 ± 3.15	
LDH (U/L)#	841.72 ± 527.41	
Ferritin (ng/mL)&	1325.42 ± 858.47	
Haemoglobin (g/dL)	12.26 ± 2.56	
Neutrophils (cell/mm3)	8056.80 ± 5052.94	
Lymphocytes (cell/mm3	1587.20 ± 1102.19	
Platelets (count/mm3)	248796.61 ± 104744.65	
Medications		
Heparin	58	98
Antibiotics	56	95
Glucocorticoids	56	95
Oseltamivir	14	26
Antimalarial	2	4
Respiratory status		
Mechanical ventilation	41	69
Nasal-cannula oxygen	59	100
pO2	79.80 ± 35.83	
SatO2	91.83 ± 9.99	
Disease severity		
Mild	0	0
Moderate	10	16.95
Severe	49	83.05
Outcome		
Death	26	44.07

**CRP: C-reactive protein (normal value <0.5 mg/dl); **D-dimers (normal value <0.5 µg/ml); #LDH lactate dehydrogenase (normal range: 120–246 U/liter); & Ferritin (normal range: 10-291 ng/ml)*